Theoretical and Applied Fracture Mechanics 141 (2026) 105245

Contents lists available at ScienceDirect

Theoretical and Applied Fracture Mechanics

journal homepage: www.elsevier.com/locate/tafmec

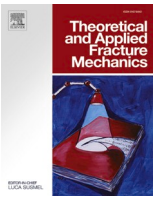

On an accurate and automated location of fatigue crack tip by analysing the displacement fields measured with digital image correlation

A. Camacho-Reyes [a,*], G.L. Gómez Gonzales [b], J.M. Vasco-Olmo [b], F.A. Diaz [b]

[a] Departamento de Física Aplicada e Ingeniería de Materiales. Escuela Técnica Superior de Ingenieros Industriales. Universidad Politécnica de Madrid, Madrid, Spain
[b] Departamento de Ingeniería Mecánica y Minera. Universidad de Jaén, Jaén, Spain

ARTICLE INFO

Keywords:
Fatigue crack growth
Crack tip location
Crack length
Crack tip displacement fields
Digital image correlation
Mathematical optimization

ABSTRACT

This paper presents two algorithms for locating the tip of growing fatigue cracks by analysing Digital Image Correlation (DIC) data. This work aims to develop algorithms that are accurate, mathematically simple, easy to implement, and computationally efficient for this purpose. In addition, the goal is to simplify experimental setups and avoid invasive techniques, thereby integrating all measurements into the DIC analysis. The algorithms are implemented by analysing the crack tip displacement fields measured by DIC, establishing the discontinuity along the crack path during fatigue propagation as the basis for estimating the accurate crack tip location. The algorithms were validated through two representative cases: a straight-growing fatigue crack in a Compact Tension specimen made of commercially pure Titanium, and an inclined-growing fatigue crack in a Double Cantilever Beam specimen made of 2024-T3 aluminium alloy. A good level of agreement has been achieved between the results obtained with the implemented algorithms and those from an alternative method, with relative deviations of approximately 2 %.

1. Introduction

Digital Image Correlation (DIC) [1] has had a significant impact on research related to fatigue crack growth. This optical technique enables full-field, non-invasive displacement and strain measurements, allowing researchers to assess key parameters that were previously unmeasurable by conventional means or to enhance the measurement and interpretation of certain mechanical parameters. Some examples of recent works include: the characterization of the shape and the size of the different plastic zones surrounding the crack tip and their influence on fatigue crack growth rates [2–5], the experimental characterization of crack tip singularity parameters such as ΔK or ΔJ through multi-point approaches [6–10], investigations on plasticity-induced crack tip shielding [11–13] and the measurement and analysis of crack tip singular displacements such COD and CTOD [14–17], among others. A common feature of these studies and, in general, of any investigation of fatigue crack growth using DIC, is the need to accurately determine the crack tip position or the path left for the crack during its fatigue propagation within the displacement maps. In this sense and beyond its influence on geometrical aspects specifically crack tracking and crack length measurement, the crack tip position may be a critical variable that can have significant influence on different aspects such as the experimentally inferred ΔK [18–21] or the measured values of COD and the identification of CTOD due to the relative position between crack flanks points and the crack tip [22]. For this reason, researchers have developed strategies and methodologies to locate the crack tip from the analysis of DIC maps. In the following, characteristic works of different methods for crack tip location from DIC data are described and discussed. As this work leads with crack tip estimation from DIC data, other approaches such as raw image processing or methods involving additional measurement equipment (potential drop, extensometer, etc) are not included below. Whilst the ΔK determination process using multi-point approaches, the crack tip location can be simultaneously estimated by including it as an unknown variable to be determined [23–26]. However, this approach involves the use of advanced numerical methods to solve a multivariable (seven variables comprising the mode I stress intensity factor, the non-singular stress, the coefficients that model the rigid body motion, and the coordinates of the crack tip for mode I Irwin-Westergaard approach [27,28]) and nonlinear optimization problem, which in addition to its high computational cost requires a well-chosen initial solution to ensure convergence. Strohmann et al. [29] developed a crack path detection

Abbreviations: DIC, Digital Image Correlation; COD, Crack Opening Displacement; CTOD, Crack Tip Opening Displacement; CT, Compact Tension Specimen; DCB, Double Cantilever Beam Specimen.

* Corresponding author.
E-mail address: alonso.camacho@upm.es (A. Camacho-Reyes).

https://doi.org/10.1016/j.tafmec.2025.105245
Received 23 July 2025; Received in revised form 10 September 2025; Accepted 16 September 2025
Available online 17 September 2025

Nomenclature

v	Vertical component of displacement field
x, y	Horizontal and vertical coordinates, respectively
α_i	Fitting polynomial coefficient $i = 1:4$
R^2	Adjusted determination coefficient
β_i	Fitting polynomial coefficient $i = 1:4$
y^i_{CP}	Vertical coordinate of the crack path for the ith profile
CV	Pearson coefficient of variation
a_n	Crack length for the n measurement
f	Image spatial calibration parameter / Pixel by millimetre ratio
X, Y	Crack tip coordinates in the image/map

algorithm using convolutional neural networks. The proposed algorithm is able to accurately identify the tip and path followed by the crack for long cracks but not for short cracks. The reason for such deviation is the inherent DIC scatter, which is significantly greater when short cracks, and therefore low stress intensity values, are under consideration. Najat et al. [30] proposed an algorithm based on the direct search of discontinuities in DIC strain maps. This approach, based on strain fields, could lead to inaccuracies in crack tip detection due to the combination of two factors: the inherent noise in displacement fields along and the gradient operators for strain tensor calculation. Owens et al. [31] employed the Canny edge detection algorithm but applied it to previously smoothed and processed DIC displacement fields to identify the crack path. Shuai et al. [32] proposed a method to mode I stress intensity factor and crack tip location estimation through the analysis of crack opening displacements along the crack flanks. Although this approach reduces computational cost by employing certain points and therefore avoids a full analysis of the displacement field, it was only validated for pure fracture mode I straight cracks. For these reasons and for the sake of efficiency, simple, computationally cheap, easy-to-implement, and effective algorithms to identify the crack tip during DIC fatigue crack growth analysis are required. In this work, two algorithms with these characteristics are presented. Both algorithms are based on the discontinuity in displacement maps caused by the presence of a fatigue crack, using the vertical displacement map as input to determine the crack tip. Unlike some previously discussed works, the direct use of the displacement field for crack tip determination avoids data pre-processing or prior calculations, which add additional processes to algorithms as well as the risk of adding excessive noise, for example, while strain calculations. Regarding the processing of the proposed algorithms, they employ simple and effective mathematical tools that simplify both implementation and calculation. Moreover, the algorithms are not restricted to specific levels of plasticity (whether small-scale or large-scale yielding), unlike those approaches that require the use of crack tip field models, which are generally elastic [23–26]. The proposed algorithms were validated on two representative case studies to demonstrate the robustness and the effectiveness of the methodology under varying geometric conditions. The first case focuses on evaluating the accuracy of the algorithms when identifying the crack tip, which is assessed by comparison with an independent measurement technique. In this case, a straight growing fatigue crack was studied. For the second study, the robustness of the algorithms was evaluated by investigating an extreme case consisting of determining the crack tip position during fatigue propagation for an inclined crack.

2. Experimental work

2.1. Case study 1: Straight growing fatigue crack

Fatigue crack growth testing was performed on a 1 mm thick CT specimen made of Grade 02 Titanium (commercially pure) at tensile constant amplitude loading. The specimen drawing is shown in Fig. 1a. For this test, a servohydraulic testing machine with a load capacity of 25 kN was employed (MTS Landmark 370.02). The loading conditions were 750 N for the maximum load with a stress ratio of 0.1 at a frequency of 10 Hz. This loading condition provides nominal stress intensity factor ranges of 17.4 and 40.5 MPa $m^{1/2}$ at the beginning and end of the test, respectively. The measurement setup consisted of two cameras, one positioned in front of the specimen to perform 2D-DIC and a second behind the specimen to control and measure the crack length during the test, as displayed in Fig. 1b.

For DIC data acquisition, a high-resolution camera (Redwood CXP 65 MP sensor provided by IO Industries) fitted to a high-magnification ultra-macro lens (LAOWA 60 mm F2.8 2×) was employed. This

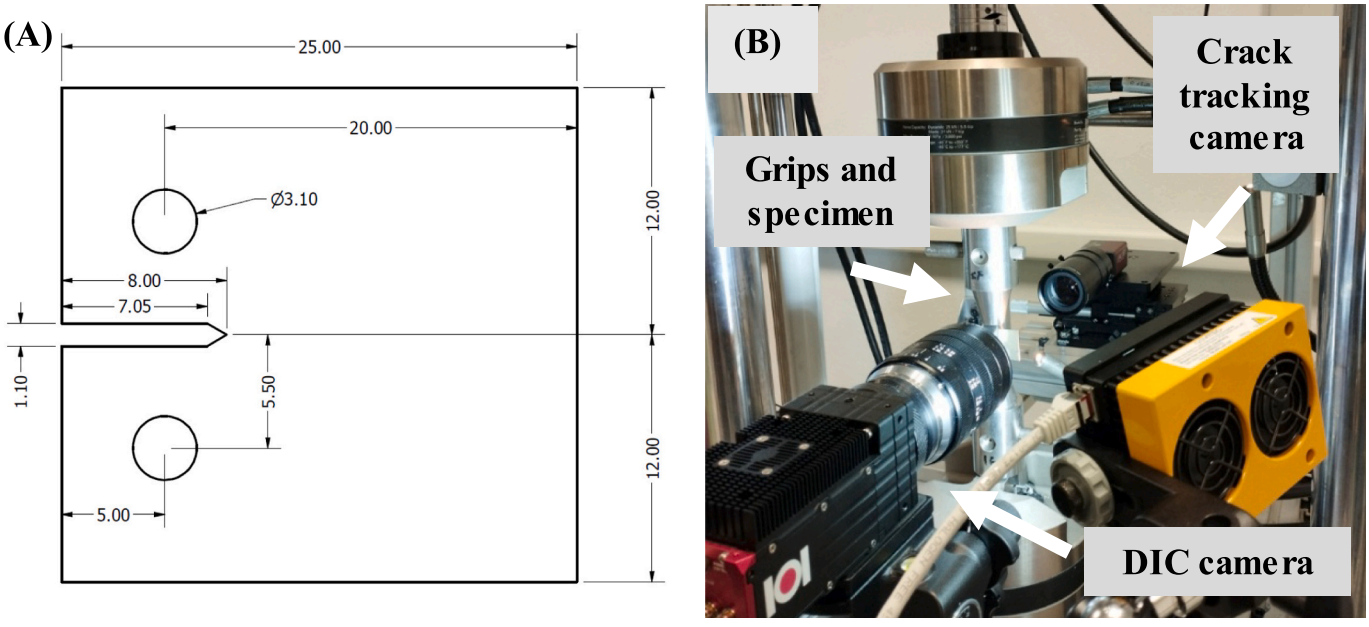

Fig. 1. a) CT Specimen drawing, b) Experimental set-up.

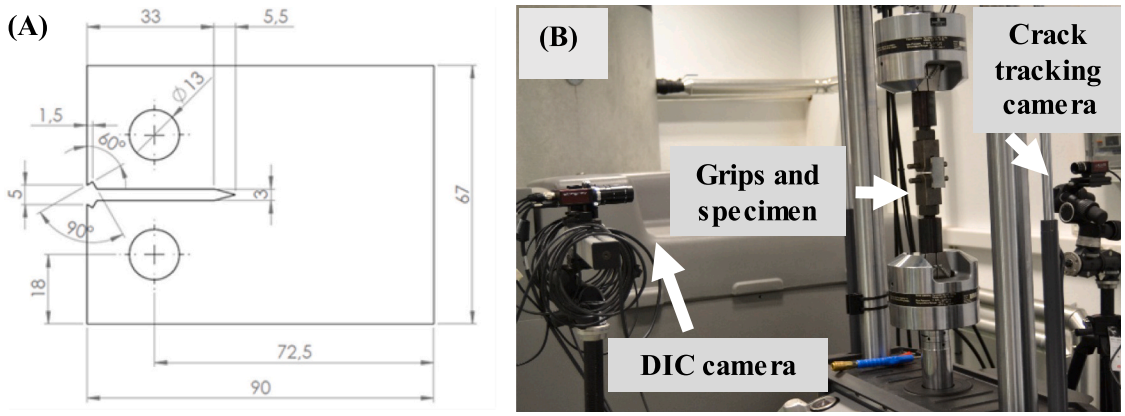

Fig. 2. a) DCB Specimen drawing, b) Experimental set-up.

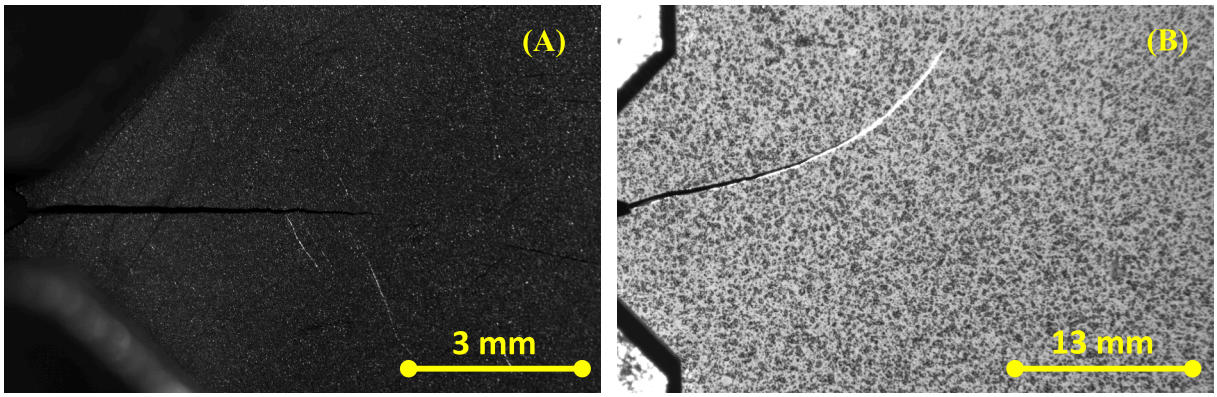

Fig. 3. DIC image captured in the last cycle before fatigue failure at the maximum load of the loading cycle showing the crack path for a) Grade 02 Titanium and b) 2024-T3 aluminium alloy specimens.

configuration results in a spatial resolution close to 2 μm per pixel. DIC images were acquired for different crack lengths, as detailed below. DIC processing was performed through commercial software VIC-2D provided by Correlated Solutions Inc. [33]. DIC processing parameters were chosen according to guidelines provided by iDICs [34]. Thus, a facet size of 31 pixels and a step value of 10 pixels were selected. For crack length control and measurements during the test, an additional camera (AVT Stingray F-504-B 5 MP sensor) fitted with a macro-zoom lens (MLH-10× EO) was mounted on a precision base driven by micrometric screws (±10 μm precision). The procedure for crack length measurement was to place the centre of the camera sensor at the crack tip and move it as the crack grows in 0.5 mm increments of length. Thus, data at 0.5 mm increments were acquired for various crack lengths within the range of 5–9 mm (measured from the load application point as defined in ASTM E647 [35]) with an uncertainty of 0.01 mm (due to micrometric screw resolution). Because the camera position changed during the location of the crack tip and, therefore, the coordinate system associated with the sensor, the synchronisation between successive coordinate systems was carried out by locating a common reference point in each system. The crack length value measured using the camera-precision base assembly was taken as a reference value to compare the inferred crack lengths using the proposed algorithms.

2.2. Case study 2: Variable inclination growing fatigue crack

In this test, fatigue crack growth testing was performed on a 2 mm thick 2024-T3 aluminium alloy Double Cantilever Beam specimen under tensile constant amplitude loading. As shown in Fig. 2a, the main difference compared to the first test specimen is the higher width-to-height ratio. The test was performed on a 100 kN servo hydraulic machine (MTS Landmark 370.10) with a loading condition of 0.1 stress ratio and 1250 N maximum load at a frequency of 10 Hz. This loading condition provides nominal stress intensity factor ranges of 15.8 and 39.8 MPa $m^{1/2}$ at the beginning and end of the test, respectively. As in the previous case, a setup consisting of two cameras placed in front of and behind the specimen was used for the simultaneous determination of DIC images and crack length measurements.

For 2D-DIC measurements, a 5 MP camera (AVT Stingray F-504-B) fitted to a 75 mm lens was employed, providing a spatial resolution of 33 μm per pixel. For crack length monitoring, a 1 MP resolution camera (AVT Pike F-032B/C) coupled to a 25 mm lens was used. In this test, the back side of the specimen was polished to improve the crack tip/path visualization and therefore their measurement using the back camera. Fig. 3 shows DIC images at the last captured cycle before fatigue failure to illustrate the fatigue crack path for both specimens, titanium (Fig. 3a) and aluminium (Fig. 3b). Regarding Fig. 3a, it should be stated that the image appears dark due to its compression for inclusion in the manuscript (original size 63 MB due to the use of a high-resolution DIC camera).

3. Description, methodology and general considerations of the algorithms

In this section, the proposed algorithms are detailed. DIC data from the first experimental test are employed to explain and illustrate the procedures and features. The main feature on which these algorithms are based is the discontinuity that is observed in the crack path when different vertical displacement profiles plotted for the area surrounding

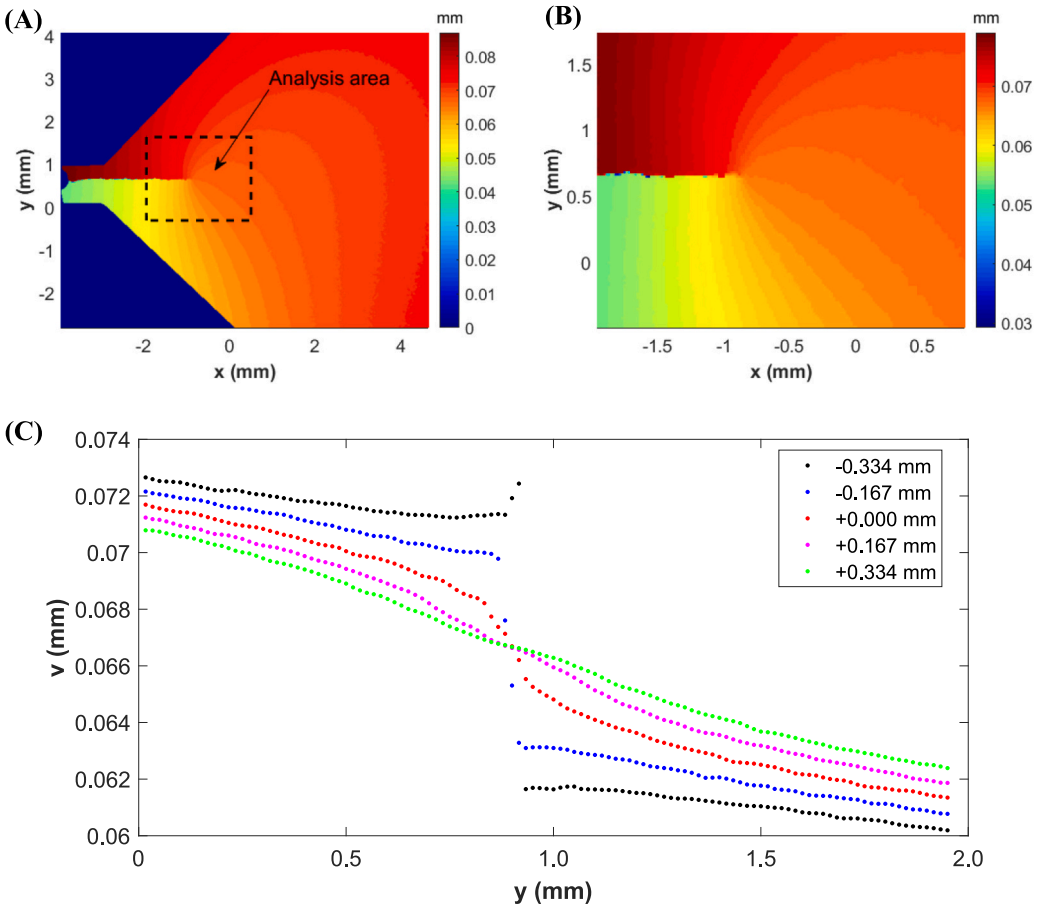

Fig. 4. a) Vertical displacement map obtained from DIC, b) detail image of the previously defined analysis area, and c) vertical displacements along the *y*-axis within the analysis region at different *x*-locations related to the estimated crack tip. Data at the maximum cycle load for a fatigue crack length of 3 mm (6 mm if defined from the load application point).

the crack tip are analysed. Thus, by identifying this discontinuity (see Fig. 4), the crack tip can be located from the analysis of the crack opening displacement maps. Other works found in the literature based on the same principle include the work of Melching et al. [36].Fig. 4a shows a vertical displacement map measured by DIC for a crack length of 6 mm (referred to the load application point as defined in ASTM E647 [35]). For convenience, in some of the following Figures, data are plotted against their position in the DIC map (image pixel divided into

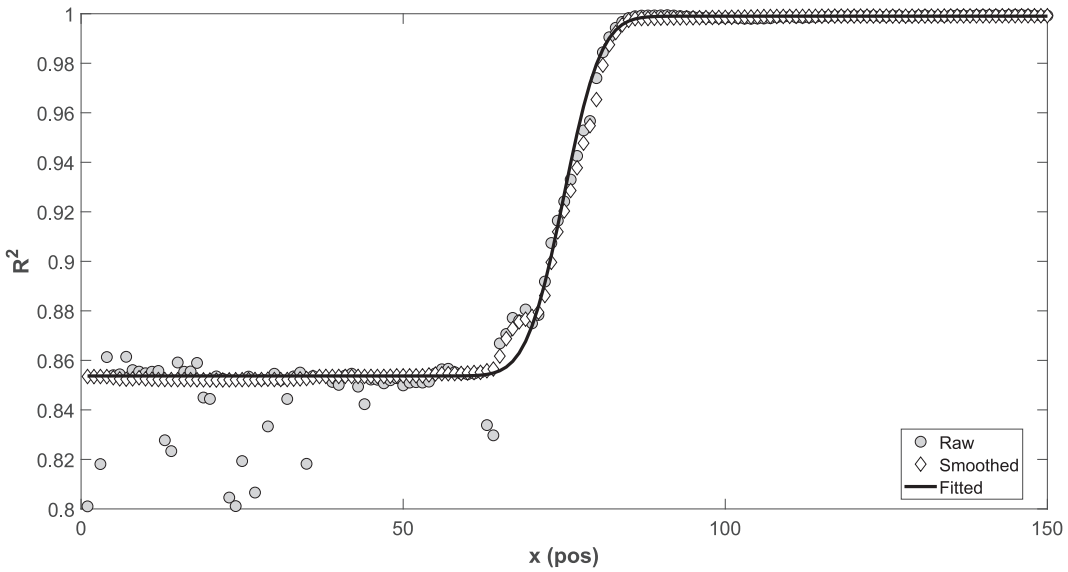

Fig. 5. Fitting quality for each vertical displacement profile along the horizontal direction. Circles represent the raw original DIC data, diamonds indicate the smoothed data, while the continuous line corresponds to the smoothed data fitted to the Gauss' error function (Eq. 2).

Table 1
Relationship between initial solution coefficients and fitted coefficients and their initial/final values.

Coefficient	Equation	Initial	Calculated
β_1	$\frac{\max R^2 - \min R^2}{2}$	0.0817	0.0729
β_2	$x \text{ at } R^2 = (\beta_1 + \beta_4)$	60.00	63.00
β_3	$\frac{x \text{ at } R^2 = 1.5 \bullet (\beta_1 + \beta_4) - x \text{ at } R^2 = 0.5 \bullet (\beta_1 + \beta_4)}{4}$	7.193	6.262
β_4	$\min R^2$	0.835	0.926

DIC processing step) instead of the distance in millimetres.

As shown in Fig. 4a and b, an interest or analysis area, which encloses the crack tip, is defined. The vertical displacement values employed for the crack tip location were extracted from such zone for several reasons. First, it avoids collecting data in the edges, which could lead to algorithm errors because of the existence of inappropriate displacement values in that zone (i.e., blue region of Fig. 4a). Secondly, the computational cost is reduced since fewer points and displacement profiles were used rather than the full map. Fig. 4c shows a set of vertical displacement profiles along the *y*-axis for different *x* locations regarding the calculated crack tip. This Figure illustrates appropriately the feature on which the proposed algorithms are based. Thus, it is clearly observed that profiles behind the crack tip (black and blue curves) present a discontinuity due to the gap that occurs at the crack path. On the other hand, for profiles at and in front of the crack tip, it is visible that each discontinuity disappears (red curve) until finally reaching an almost linear trend (magenta and green curves). The proposed algorithms are detailed in the following subsections.

3.1. Algorithm 1. Algorithm based on the inflection point

This algorithm is based on finding the inflection point that occurs at the crack tip, as displayed in Fig. 4c. Thus, based on the idea above described, the crack tip can be found as the first highest fitting quality point. For that, a mathematical function to model this feature is necessary. A cubic polynomial was used to fit the displacement profiles plotted along the *y*-axis, as shown in Eq. 1. In contrast to previous work, such as Melching et al. [36], which uses a hyperbolic tangent function, the use of a cubic function simplifies the start of the algorithm, as it does not require the use of numerical methods for fitting.

$$v(y) = \alpha_1 + \alpha_2 y + \alpha_3 y^2 + \alpha_4 y^3 \tag{1}$$

Where v is the vertical displacement value and α_i are the polynomial coefficients, with $i = 1:4$. This polynomial function allows for using a linear least square fitting as well as obtaining the inflection point (Eq. 1 second derivative equal to 0) by combining the third and fourth order coefficients as follows: $-\alpha_3/3\alpha_4$. The adjusted R^2 determination coefficient was used as a fitting quality parameter. Fig. 5 shows the obtained fitting quality parameter for the different displacement profiles along the crack growth direction (*x*-axis).

As shown in Fig. 5, the fitting quality parameter exhibits a sigmoidal shape, and the dispersion of the first points may be fairly attributed to crack path discontinuity, which may provide irregular results in terms of fitting. As it may be inferred from Fig. 4c, when the fitting quality parameter reaches a value close to unity, the crack tip is found since that displacement profile exhibits a cubic trend. The good-fitting quality for the profiles ahead of the crack tip is due to their linear trend, which can be well fitted by a cubic polynomial. At this point, by choosing the *x*-position of the best first fitting quality point and subsequently the calculation of the inflection point at such position, the *x* and *y* crack tip coordinates would be obtained. However, it is not numerically simple to get that point since the following problems may appear. When choosing a target value for the R^2 parameter to get the *x* crack tip coordinate (99 % in this work), a problem of duality values may appear since R^2 values ahead of the crack tip are similar. Hence, a nearest neighbour interpolation to the target value could lead to an error or a different value. In addition, if for any reason such inherently noisy experimental values do not reach values close to unity, the algorithm may also be misled. Thus, one way to proceed that avoids these problems is to fit R^2 data to a sigmoidal function, which also allows data normalisation (values varying between 0 and 1) and operating with it instead of using raw data. For convenience, Gauss' error function [37] was chosen as the sigmoidal function, as shown in Eq. 2.

$$R^2 = \beta_1 \mathrm{erf}\left(\frac{x - \beta_2}{\beta_3}\right) + \beta_4 \tag{2}$$

Where erf indicates Gauss' error function, β_1 is the amplitude coefficient, β_2 is the *x*-offset coefficient, β_3 is a scaling coefficient, and β_4 is the *y*-offset coefficient. The fitting of R^2 data to that function implies solving a nonlinear fitting problem and therefore an initial solution problem. However, from observation and interpretation of experimental plotted data, a well-chosen initial solution (close to the solution) can be obtained since the Eq. 2 coefficients can be obtained with reasonable accuracy (see Table 1). As the raw data contains some points out of trend, especially at the crack path because of the crack tip discontinuity, as shown in Fig. 5, it is desirable to derive the initial solution from smoothed data as shown in Fig. 5. Data smoothing was performed using the median filter implemented in the Matlab function *smoothdata* [38]. The initial solution values as a function of smoothed R^2 data are displayed in Table 1. Once the initial solutions were defined, the nonlinear fitting was performed using the Levenberg-Marquardt algorithm [39–41]. For example, Table 1 also shows the initial and the finally calculated error function coefficients, and the fitted function is displayed in Fig. 5.

Once the fitted function has been obtained, to avoid issues because of the numerical values of R^2 as previously described, fitted *y*-axis data is normalised using the obtained coefficients β_1 and β_4, and then, the *x*-coordinate of the crack tip is extracted for a normalised R^2 value of 0.99. Hence, for such an *x*-profile, the *y*-coordinate of the crack tip is calculated as the inflection point of the fitted cubic polynomial. Thus, these values for the example case are: *X* equal to 190 units in the map (4210 pixels in the image), *Y* equal to 204 units in the map (3084 pixels in the image) which provide an estimated crack length of 6.09 mm (reference crack length of 6.00 mm).

3.2. Algorithm 2. Algorithm based on crack path displacement gradient

This algorithm is based on identifying the highest gradient that occurs at the crack path due to the crack discontinuity. As inferred from Fig. 4c, the crack path can be identified by locating the maximum gradient point of each displacement profile. Thus, the *y*-coordinate of the gap left by the crack in the displacement map is given by:

$$y^i_{CP} = \max(|\nabla v(y)|) \tag{3}$$

In this Equation, y^i_{CP} is the *y*-coordinate of the crack path for the *i*-th displacement profile, ∇ is the gradient operator, and vertical bars represent the absolute value. Regarding the calculation of the gradient in the above expression, it should be noted that, as is common when strain calculation from DIC data, a strain window was not defined or used. When using vertical profiles, the gradient corresponds to the

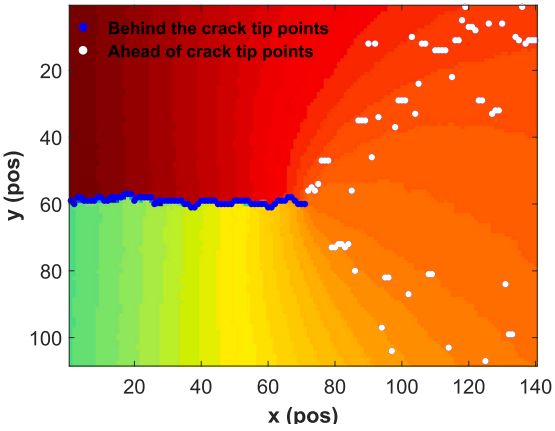

Fig. 6. Maximum gradient point of each displacement profile y^i_{CP}.

derivative in the direction of the profile. Fig. 6 shows the calculated values of y^i_{CP} for a crack length of 6 mm. As shown in this Figure, the crack path can be easily recognised from the direct calculation of this value. Hence, the crack tip can be easily identified visually by choosing the last crack path point (the last point before the dispersed trend in Fig. 6). Nevertheless, as the purpose of this paper is to automate crack tip calculations, it is essential to identify a suitable method for the automatic extraction of the crack tip, which is not straightforward, as will be discussed below. The crack tip can be located through the identification of both zones shown in Fig. 6. For this purpose, an analysis of such data based on the statistical dispersion was performed.

A cumulative mean and standard deviation were calculated for each point as the mean and standard deviation of all the preceding data up to the chosen point. For those points, the deviation coefficient (standard deviation divided by the mean value) was computed in order to work with a dimensionless value, which allows a more generic analysis to be performed. Fig. 7a shows the calculated crack path *y*-coordinate, whereas Fig. 7b shows the calculated cumulative deviation coefficient for that data.

As shown in Fig. 7, two different zones (crack path and outside crack path) can be observed in terms of the deviation coefficient. As depicted in the figure, two linear trends were observed: the first, characterized by a nearly zero slope line (constant), and the second, represented by a line with a positive slope. As can be inferred from Fig. 7a and b, the constant dispersion zone corresponds to the crack path, and the increasing dispersion zone to the crack path outside zone. Regarding the behaviour outside the crack path, the statistical variability outside the crack path is since the vertical displacement in that area being linear, which generates maximum gradient points with no physical significance and increases the relative cumulative distortion. Hence, the boundary between both zones provides the *x*-coordinate of the crack tip. At this stage, a suitable method to identify such point should be found. A simple idea is to define a limit for the deviation coefficient. Thus, as the deviation coefficient reaches that value, the *x*-coordinate of the crack tip can be considered as found. From the observation and analysis of the experimental data, a 2 % deviation value was chosen which was obtained by a sensitive analysis of the data. However, this idea may not be generalisable to other situations, and it would be susceptible to failure if there were any points out of trend due to the inherent experimental noise, among others. An alternative method to locate the *x*-coordinate of the crack tip, avoiding the above-mentioned problems, lies in the mathematical characterization of both zones (constant and increasing lines) by using linear least squares fitting. Thus, the two regions are fitted and the *x*-coordinate of the crack tip is obtained by determining the intersection point between both fitted lines. The initial set of data to be fitted for the first region was derived from selected data exhibiting a variation coefficient ranging from 0 to 2 %, while the data for the second region was obtained from values falling within the 2 to 10 % range. The identified crack tip, as well as both fitted lines superimposed over the raw data, are displayed in Fig. 8. Once the *x*-coordinate of the crack tip has been identified, the *y*-coordinate is directly obtained for such a point from Fig. 7a data. Hence, the obtained values using this algorithm are: *X* equal to 189 units in the map (4200 pixel in the image), *Y* equal to 203 units in the map (3074 pixel in the image), which provide an estimated crack length of 6.07 mm (reference crack length of 6.00 mm).

4. Validation of the algorithms and discussion of results

4.1. Straight growing crack

In this case study, where the crack grew straight, the inferred crack length was calculated as the difference between the *x* coordinate of the calculated crack tip and the *x* coordinate of the specimen edge. Fig. 9a shows the estimated crack length against the reference crack length for the different proposed algorithms. In this Figure, a 45-degree line has been included to verify the level of agreement between the data. Fig. 9b shows the relative error in absolute value against the reference crack length for both proposed algorithms. These results, along with the normalised crack length (crack length divided by the specimen width), are numerically expressed in Table 2. As shown in the above-mentioned Figures, both algorithms show a good agreement since the relative deviation from the reference value is less than 2 % for any algorithm and any analysed crack length. Such a small deviation is also observed in

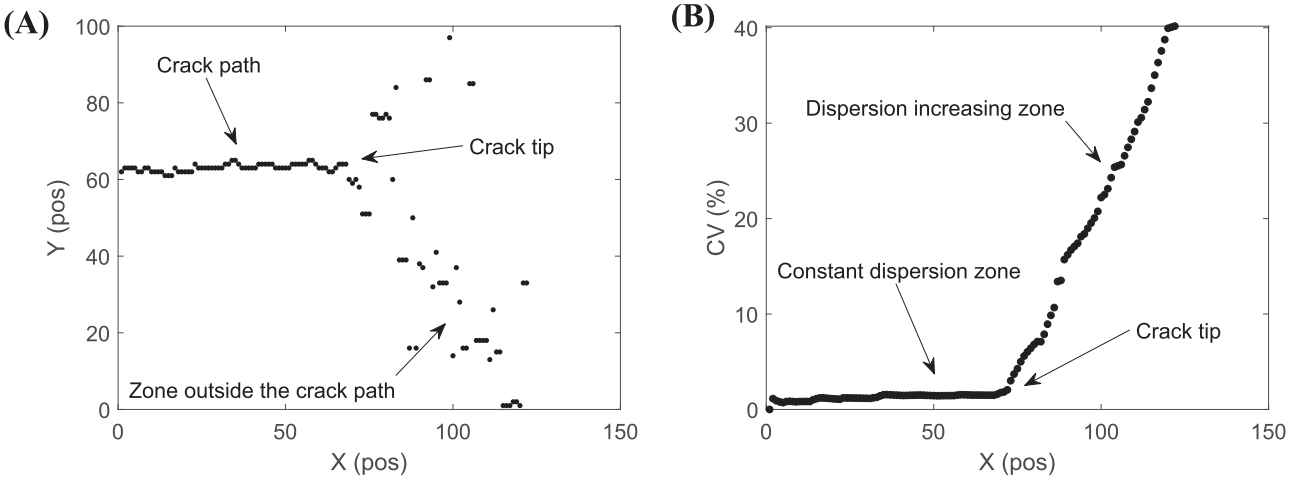

Fig. 7. a) Calculated crack path y-coordinate and b) % variation coefficient for the cumulative data.

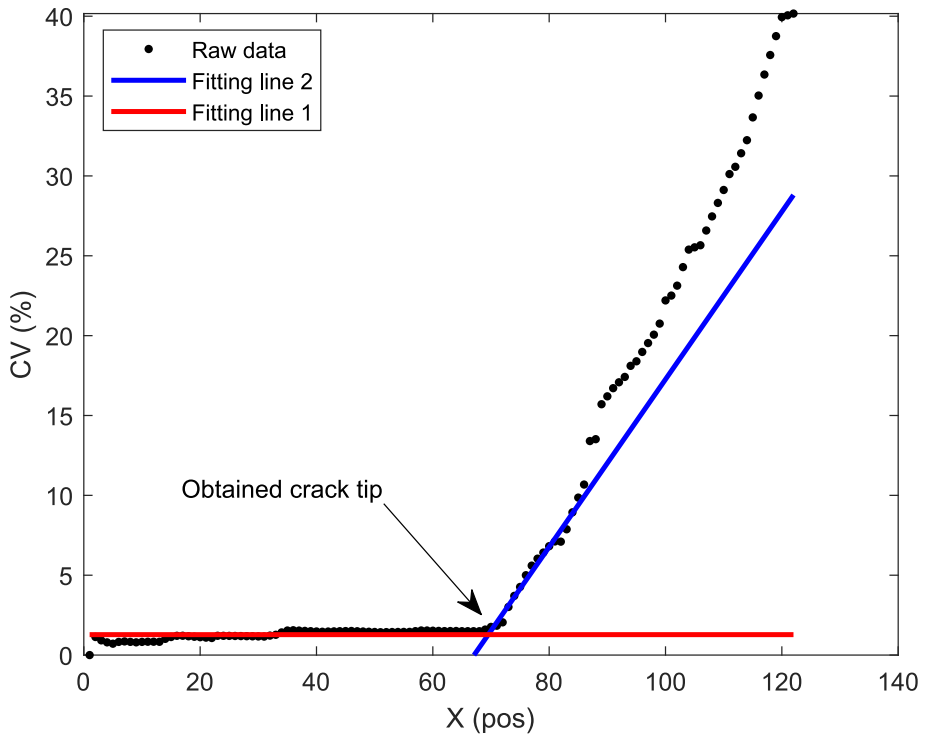

Fig. 8. Plot to illustrate how to obtain the crack tip from the intersection of both dispersion zones.

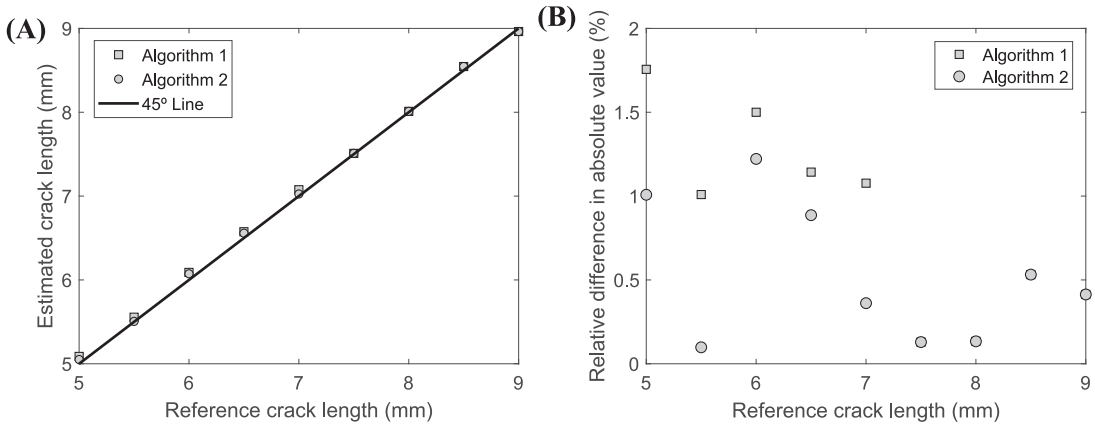

Fig. 9. a) Calculated crack length against reference crack length and b) absolute difference between calculated and reference crack lengths against the reference crack length. Grade 02 Titanium specimen.

Table 2
Reference and calculated crack length values along with the relative difference in percentage between them for the Grade 02 Titanium specimen.

Reference crack length		Algorithm 1		Algorithm 2	
(mm)	(a/W)	(mm)	(%)	(mm)	(%)
5.00	0.250	5.09	1.76	5.05	1.01
5.50	0.275	5.56	1.01	5.51	0.10
6.00	0.300	6.09	1.50	6.07	1.22
6.50	0.325	6.57	1.14	6.56	0.89
7.00	0.350	7.08	1.08	7.03	0.36
7.50	0.375	7.51	0.13	7.51	0.13
8.00	0.400	8.01	0.13	8.01	0.13
8.50	0.425	8.55	0.53	8.55	0.53
9.00	0.450	8.96	0.41	8.96	0.41
		Deviation Avg ± Std		Deviation Avg ± Std	
		0.85 ± 0.58		0.54 ± 0.42	

Fig. 9a, where all of the data fairly fall on a 45° line. Regarding the accuracy of each algorithm in this case study, no significant differences were detected in terms of the estimated crack length since the maximum deviation between algorithms for a given crack length is around 1 %.

Fig. 10 displays the inferred crack tips using both algorithms superimposed over the reference speckle image at the longest measured crack length of 9 mm (before fatigue failure). This Figure shows graphically the goodness and the accuracy of the proposed algorithms when determining the crack tip position since all the calculated points fairly follow the crack path illustrated in that image. Please note that in this image, there may be a slight graphical difference between the gap left by the crack and the point calculated due to the crack growth itself, especially for the points furthest away from the last measured crack tip. However, in no case does this indicate inaccuracy or a high deviation of the algorithm.

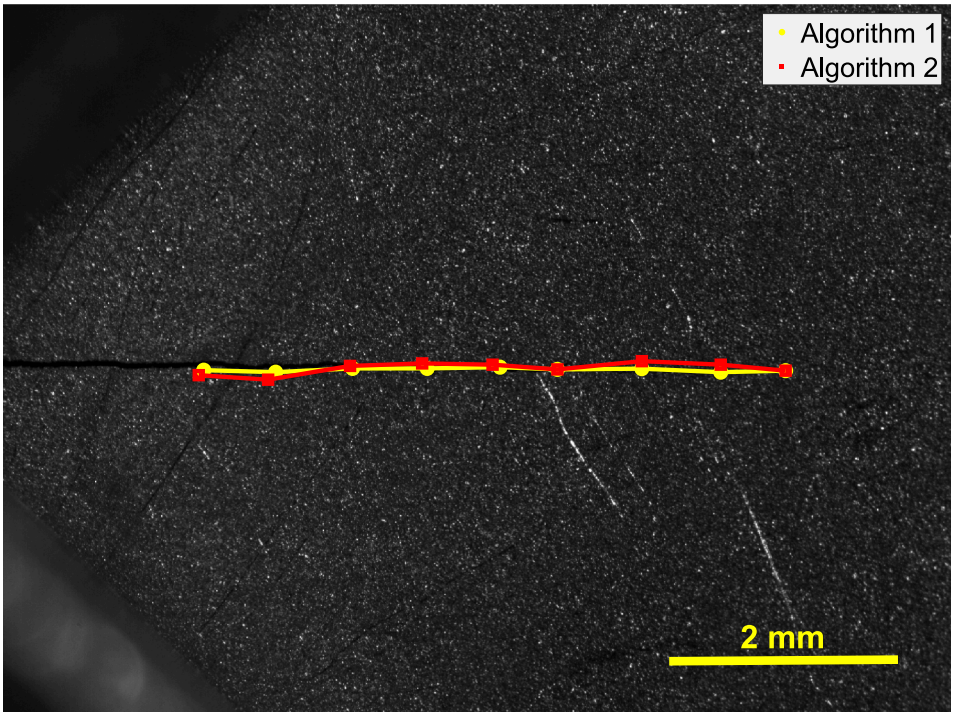

Fig. 10. Inferred crack tips superimposed over the speckle reference image (unloaded state) corresponding to the longest measured crack length before fatigue failure. Grade 02 Titanium specimen. Yellow squares correspond to Algorithm 1, whilst red circles correspond to Algorithm 2. (For interpretation of the references to colour in this figure legend, the reader is referred to the web version of this article.)

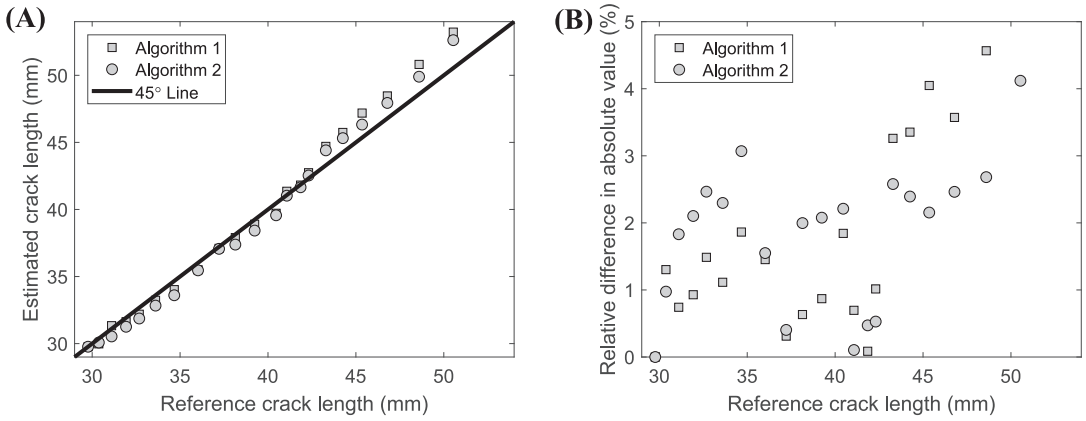

Fig. 11. a) Calculated crack length against reference crack length and b) absolute difference between calculated and reference crack lengths against the reference crack length. 2024-T3 aluminium alloy specimen.

4.2. Crack growing with variable inclination

In this test, as the crack grew with variable inclination, the crack length was calculated as the cumulative Euclidean distance between successive estimated crack tips, as shown in Eq. 4. In that equation, f is the spatial calibration parameter in pixel by millimetre, n is the number of measured crack lengths, i is the sum index, and X and Y are the calculated horizontal and vertical crack tip coordinates on the DIC image in pixels, respectively. The reference crack length, which was used for comparison and validation, was calculated in the same way and for the same points.

$$a_n = f \bullet \sum_{i=2}^{n} \left((X_i - X_{i-1})^2 + (Y_i - Y_{i-1})^2 \right)^{1/2} \quad (4)$$

Fig. 11a shows the calculated crack lengths against the reference crack for the different proposed algorithms. In this Figure, a 45-degree line has been included to check the matching between both data and to assist the graph interpretation. As inferred from this Figure, all the points fairly fall on the 45-degree line, which means a good agreement between both calculated and reference crack length values. For the last values of the series, the deviation from the first values increases slightly. However, such deviation is still acceptable as discussed below. Fig. 11b, which shows the relative difference in absolute value between reference and calculated values, establishes a quantitative comparison between those values. Values represented in Fig. 11 together with the normalised crack length can be found in Table 3. As inferred from Fig. 11b, good values in terms of relative deviation are obtained. The average relative deviation for Algorithm 1 is 1.92 % with a standard deviation of 1.53 % whilst for Algorithm 2, the average relative deviation is 1.92 with a standard deviation of 1.00 %. From the above exposed results, it may be stated that both algorithms are accurate in terms of crack tip and length determination, also for an inclined fatigue crack with variable slope.

Table 3
Reference and calculated crack length values along with the relative difference in percentage between them for the 2024-T3 aluminium specimen.

Reference crack length		Algorithm 1		Algorithm 2	
(mm)	(a/W)	(mm)	(%)	(mm)	(%)
30.38	0.419	29.98	1.30	30.08	0.98
31.10	0.429	31.34	0.74	30.53	1.83
31.93	0.440	31.63	0.93	31.26	2.10
32.68	0.451	32.19	1.49	31.87	2.47
33.60	0.464	33.23	1.11	32.83	2.30
34.67	0.478	34.02	1.86	33.60	3.07
36.02	0.497	35.50	1.45	35.46	1.55
37.22	0.513	37.10	0.31	37.07	0.40
38.14	0.526	37.90	0.63	37.38	2.00
39.24	0.541	38.90	0.87	38.43	2.08
40.46	0.558	39.71	1.84	39.57	2.21
41.07	0.566	41.36	0.70	41.03	0.10
41.85	0.577	41.82	0.09	41.66	0.47
42.31	0.584	42.74	1.01	42.53	0.53
43.29	0.597	44.70	3.26	44.41	2.58
44.26	0.610	45.74	3.35	45.32	2.39
45.35	0.626	47.19	4.05	46.33	2.15
46.79	0.645	48.46	3.57	47.94	2.46
48.59	0.670	50.81	4.57	49.90	2.68
50.54	0.697	53.22	5.31	52.62	4.12
		Deviation Avg ± Std		Deviation Avg ± Std	
		1.92 ± 1.53		1.92 ± 1.00	

Fig. 12 shows the inferred crack tips from both algorithms superimposed over the DIC reference image corresponding to the maximum measured crack length. This figure demonstrates the accuracy of both proposed algorithms, showing that both the calculated crack tips and the crack path due to fatigue propagation closely match.

4.3. General comparison and discussion

To establish a comparison between both case studies and the proposed algorithms, Fig. 13 shows both the normalised estimated crack length and the relative difference in absolute against the normalised reference crack length value for both materials and algorithms. Although all deviation values are acceptable as previously discussed, in general terms, deviations for the first case study are lower than for the second case study, averaging around 1 %. This small difference is explained by the spatial resolution achieved in each test. Thus, a higher resolution, as in the first case study, should provide results with a lower deviation. This is also supported by the coefficients of variation (the relationship between average and standard deviation) of each data set, which are similar (around 0.6). According to this, if the resolution effect is removed by normalising statistical results, those normalised dispersion results for both case studies are similar. Regarding the deviations provided by Algorithm 1 for both tests, even following the trend mentioned above, similar values were found except for a few points corresponding to normalised crack lengths between 60 and 70 %. In contrast, for Algorithm 2, the deviations are slightly different depending on the case study and the normalised crack length value. Thus, from the above, it can be concluded that Algorithm 1 is slightly more precise than Algorithm 2. This can be attributed to the use of smoothing and curve-fitting techniques in the first algorithm, which may help mitigate inaccuracies caused by the inherent experimental noise present in the displacement data.

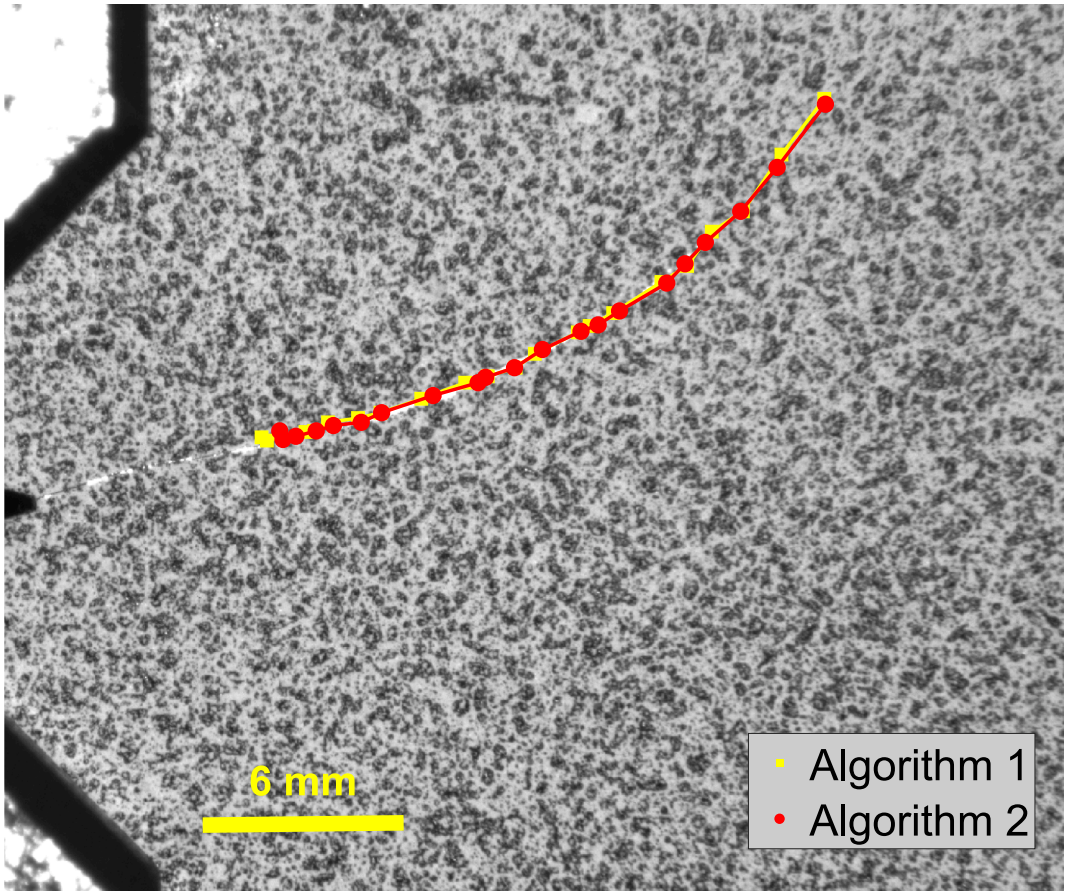

Fig. 12. Inferred crack tips superimposed over the DIC reference image (unloaded state) corresponding to the maximum measured crack length before fatigue failure. 2024-T3 aluminium alloy specimen. Yellow squares correspond to Algorithm 1, whilst red circles correspond to Algorithm 2. (For interpretation of the references to colour in this figure legend, the reader is referred to the web version of this article.)

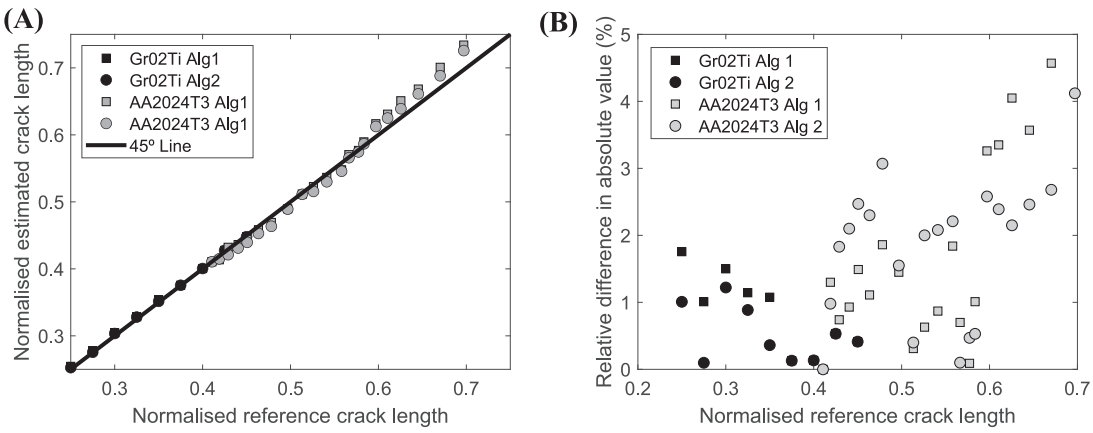

Fig. 13. a) Normalised estimated crack length and b) relative deviation in absolute value against the normalised crack length for both materials and algorithms.

As shown in Fig. 13b, the highest deviations were found for larger crack lengths, specifically values between 0.6 and 0.7. Nonetheless, those deviation values were still acceptable (around 3 %). This increase in deviation in the longer crack lengths might be due to the specimen edge effect, since in these cases the ligament is small and the field surrounding the crack tip could be affected by the edge. Lastly, it is worth mentioning that both algorithms have been tested and therefore validated over a wide range of normalised crack lengths (~20–70 %). This range covers practically 100 % of crack lengths encountered in practice, as for a CT specimen, values below 20 % correspond to cracks whose length is less than the uncracked specimen notch, while values above 70 % are less frequent. However, there is no a priori technical limitation of the algorithms for higher and lower normalised crack lengths, if the case may arise.

5. Conclusions

In this work, two algorithms for determining the crack tip and the crack path from DIC data have been developed and validated for two representative cases: a straight-growing fatigue crack in a CT specimen made of Grade 02 Titanium, and an inclined-growing fatigue crack in a DCB specimen made of 2024-T3 aluminium alloy. Both algorithms demonstrate good results in terms of crack tip and length determination, providing average deviations of around 2 % compared to an alternative method. These algorithms, based on the direct analysis of the measured DIC data, are accurate, robust, computationally cheap, and easy to implement. Another important advantage is that the proposed algorithms are not constrained by plasticity effects (under either small- or large-scale yielding conditions), unlike approaches that rely on crack tip field models. As tools for crack tip tracking and length measurements, these algorithms can simplify and improve the experimental laboratory work on fatigue crack growth, in comparison with other conventional methods, which are usually invasive. According to this, an integral analysis of fatigue crack growth can be performed exclusively with the use of the DIC technique. In addition, the proposed algorithms enable a more precise analysis of parameters such as ΔK, ΔJ, or relative displacements along the crack flanks (ΔCOD, ΔCTOD, etc), allowing for improved understanding of their influence on fatigue crack growth. Therefore, the proposed algorithms are an effective complement to experimental fracture mechanics investigations, where an accurate and effective location of the crack tip is a crucial aspect.

CRediT authorship contribution statement

A. Camacho-Reyes: Writing – original draft, Writing – review & editing, Visualization, Software, Methodology, Investigation, Formal analysis, Funding acquisition, Conceptualization. **G.L. Gómez Gonzales:** Writing – review & editing, Validation, Software, Methodology. **J.M. Vasco-Olmo:** Writing – review & editing, Validation, Supervision, Methodology. **F.A. Diaz:** Supervision, Writing – review & editing.

Declaration of competing interest

The authors declare that they have no known competing financial interests or personal relationships that could have appeared to influence the work reported in this paper.

Acknowledgements

The authors acknowledge to Escuela Técnica Superior de Ingenieros Industriales de la Universidad Politécnica de Madrid for the financial support through the research project with reference code 'D05ACR25 ETSII-UPM25-PU01' in the program 'Primeros Proyectos 2025' without this work could not been performed. The authors also gratefully acknowledge the financial support provided by the Universidad de Jaén through its Plan Operativo de Apoyo a la Investigación (POAIUJA).

Data availability

Data will be made available on request.

References

[1] H. Schreier, J.J. Orteu, M.A. Sutton, Image Correlation for Shape, Motion and Deformation Measurements: Basic Concepts, Theory and Applications, Springer US, 2009, https://doi.org/10.1007/978-0-387-78747-3.
[2] M. Besel, E. Breitbarth, Advanced analysis of crack tip plastic zone under cyclic loading, Int. J. Fatigue 93 (2016) 92–108, https://doi.org/10.1016/j.ijfatigue.2016.08.013.
[3] X. Zhao, J. Li, J.-M. Ge, T. Sun, H. Deng, J.-G. Zhu, Determination of fatigue crack tip location and plastic zone dimensions using displacement fields measured by digital image correlation method, Eng. Fract. Mech. 320 (2025) 111060, https://doi.org/10.1016/j.engfracmech.2025.111060.
[4] J. Hosdez, M. Langlois, J.-F. Witz, N. Limodin, D. Najjar, E. Charkaluk, P. Osmond, A. Forre, F. Szmytka, Plastic zone evolution during fatigue crack growth: digital image correlation coupled with finite elements method, Int. J. Solids Struct. 171 (2019) 92–102, https://doi.org/10.1016/j.ijsolstr.2019.04.032.
[5] X. Zhao, J. Li, T. Sun, H. Deng, J.-G. Zhu, M.-Y. Tang, Y.-K. Li, Characterization of fatigue crack growth rate by digital image correlation measurements of the plastic zone considering multiple parameters, Eng. Fract. Mech. 315 (2025) 110814, https://doi.org/10.1016/j.engfracmech.2025.110814.
[6] E. Breitbarth, T. Strohmann, G. Requena, High-stress fatigue crack propagation in thin AA2024-T3 sheet material, Fatigue Fract. Eng. Mater. Struct. 43 (2020) 2683–2693, https://doi.org/10.1111/FFE.13335.
[7] Z. Zhang, B. Yang, S. Wang, S. Xiao, G. Yang, T. Zhu, A fatigue crack tip field model considering residual stress and plasticity-induced closure for welded structures, Eng. Fract. Mech. 307 (2024) 110297, https://doi.org/10.1016/j.engfracmech.2024.110297.
[8] J. Li, B. Yang, S. Wang, M.N. James, S. Xiao, T. Zhu, G. Yang, Modified model of crack tip stress field considering dislocation slip accumulation and crack tip

blunting, Chin. J. Mech. Eng. 36 (2023) 1–14, https://doi.org/10.1186/S10033-023-00875-9, 36:1.
[9] F. Paysan, E. Dietrich, E. Breitbarth, A robot-assisted microscopy system for digital image correlation in fatigue crack growth testing, Exp. Mech. (2023), https://doi.org/10.1007/s11340-023-00964-9.
[10] B. Lin, S. Alshammrei, T. Wigger, J. Tong, Characterisation of fatigue crack tip field in the presence of significant plasticity, Theor. Appl. Fract. Mech. 103 (2019) 102298, https://doi.org/10.1016/J.TAFMEC.2019.102298.
[11] F. Paysan, D. Melching, E. Breitbarth, Plasticity-induced crack closure identification during fatigue crack growth in AA2024-T3 by using high-resolution digital image correlation, Int. J. Fatigue 192 (2025) 108703, https://doi.org/10.1016/j.ijfatigue.2024.108703.
[12] J. Tong, Full-field characterisation of crack tip deformation and fatigue crack growth using digital image correlation—a review, Fatigue Fract. Eng. Mater. Struct. 41 (2018) 1855–1869, https://doi.org/10.1111/ffe.12859.
[13] A. Camacho-Reyes, J.M. Vasco-Olmo, G.L. Gómez Gonzales, F.A. Diaz, Study of effective stress intensity factor through the CJP model using full-field experimental data, Materials 16 (2023) 5705, https://doi.org/10.3390/MA16165705, 2023, Vol. 16, Page 5705.
[14] M.A. Sutton, J.H. Yan, X. Deng, C.S. Cheng, P. Zavattieri, Three-dimensional digital image correlation to quantify deformation and crack-opening displacement in ductile aluminum under mixed-mode I/III loading, Opt. Eng. 46 (2007) 051003, https://doi.org/10.1117/1.2741279.
[15] M.A. Verstraete, R.M. Denys, K. Van Minnebruggen, S. Hertelé, W. De Waele, Determination of CTOD resistance curves in side-grooved single-edge notched tensile specimens using full field deformation measurements, Eng. Fract. Mech. 110 (2013) 12–22, https://doi.org/10.1016/j.engfracmech.2013.07.015.
[16] T. Strohmann, D. Melching, F. Paysan, E. Dietrich, G. Requena, E. Breitbarth, Next generation fatigue crack growth experiments of aerospace materials, Sci. Rep. 14 (2024) 14075, https://doi.org/10.1038/s41598-024-63915-x.
[17] M. Ajmal, C. Lopez-Crespo, A.S. Cruces, P. Lopez-Crespo, New plastic crack-tip opening displacement tool based on digital image correlation for estimating the fatigue-crack-growth law on 316L stainless steel, Materials 16 (2023) 4589, https://doi.org/10.3390/ma16134589.
[18] B. Yang, Z. Wei, Z. Liao, S. Zhou, S. Xiao, T. Zhu, G. Yang, M. Wang, Optimisation method for determination of crack tip position based on Gauss-Newton iterative technique, Chin. J. Mech. Eng. (English Edition) 34 (2021) 70, https://doi.org/10.1186/s10033-021-00585-0.
[19] M. Zanganeh, P. Lopez-Crespo, Y.H. Tai, J.R. Yates, Locating the crack tip using displacement field data: a comparative study, Strain 49 (2013) 102–115, https://doi.org/10.1111/str.12017.
[20] A. Camacho-Reyes, J.M. Vasco-Olmo, M.N. James, F.A. Diaz, Towards a new methodology for the characterisation of crack tip fields based on a hybrid computational approach, Int. J. Fatigue (2022) 106942, https://doi.org/10.1016/j.ijfatigue.2022.106942.
[21] J.R. Yates, M. Zanganeh, Y.H. Tai, Quantifying crack tip displacement fields with DIC, Eng. Fract. Mech. 77 (2010) 2063–2076, https://doi.org/10.1016/j.engfracmech.2010.03.025.
[22] J.M. Vasco-Olmo, F.A. Diaz, F.V. Antunes, M.N. James, Characterisation of fatigue crack growth using digital image correlation measurements of plastic CTOD, Theor. Appl. Fract. Mech. 101 (2019) 332–341, https://doi.org/10.1016/j.tafmec.2019.03.009.
[23] S. Yoneyama, Y. Morimoto, M. Takashi, Automatic evaluation of mixed-mode stress intensity factors utilizing digital image correlation, Strain 42 (2006) 21–29, https://doi.org/10.1111/j.1475-1305.2006.00246.x.
[24] F. Mathieu, F. Hild, S. Roux, Identification of a crack propagation law by digital image correlation, Int. J. Fatigue 36 (2012) 146–154, https://doi.org/10.1016/j.ijfatigue.2011.08.004.
[25] M. Zhang, M. Shen, D. Li, M. He, Y. Li, A method for determining crack tip location during the tuff crack propagation based on ultra-fast time resolution method and immune algorithm, Eng. Fract. Mech. 321 (2025) 111129, https://doi.org/10.1016/j.engfracmech.2025.111129.
[26] B.V. Farahani, F. Direito, P.J. Sousa, P.J. Tavares, V. Infante, P.P.M.G. Moreira, Crack tip monitoring by multiscale optical experimental techniques, Int. J. Fatigue 155 (2022) 106610, https://doi.org/10.1016/j.ijfatigue.2021.106610.
[27] H.M. Westergaard, Bearing pressures and cracks, J. Appl. Mech. 61 (1939) 49–53.
[28] G.R. Irwin, Analysis of stresses and strains near the end of a crack traversing plate, J. Appl. Mech. 24 (1957) 361–370.
[29] T. Strohmann, D. Starostin-Penner, E. Breitbarth, G. Requena, Automatic detection of fatigue crack paths using digital image correlation and convolutional neural networks, Fatigue Fract. Eng. Mater. Struct. 44 (2021) 1336–1348, https://doi.org/10.1111/ffe.13433.
[30] Z. Najat, M. Fatima, H. Taoufik, T. Yassine, R. Rajaa, M. Ibrahim, R. Hassan, Improvement of crack tip position estimation in DIC images by image processing methods, Frattura Ed Integrita Strutturale 17 (2023) 61–71, https://doi.org/10.3221/IGF-ESIS.63.06.
[31] A. Taylor Owens, H.V. Tippur, An image processing technique to identify crack tip position and Automate fracture parameter extraction using DIC: application to dynamic fracture, Exp. Mech. 63 (2023) 445–466, https://doi.org/10.1007/s11340-022-00925-8.
[32] J. Shuai, J. Zhao, L. Lei, Simple crack tip and stress intensity factor determination method for model I crack using digital image correlation, Theor. Appl. Fract. Mech. 122 (2022) 103621, https://doi.org/10.1016/j.tafmec.2022.103621.
[33] Correlated Solutions, (n.d.). www.correlatedsolutions.com.
[34] I. Jones, R. Bigger, B. Blaysat, C. Boo, M. Grewer, J. Hu, A. Jones, M. Klein, K. Raghavan, P. Reu, T. Schmidt, T. Siebert, M. Simenson, D. Turner, A. Vieira, T. Weikert, A Good Practices Guide for Digital Image Correlation, 2018, https://doi.org/10.32720/idics/gpg.ed1.
[35] ASTM, E 647–00: Standard Test Method for Measurement of Fatigue Crack Growth Rates 11, Annual Book of ASTM Standards, 2000, p. 03.
[36] D. Melching, F. Paysan, T. Strohmann, E. Breitbarth, An iterative crack tip correction algorithm discovered by physical deep symbolic regression, Int. J. Fatigue 187 (2024) 108432, https://doi.org/10.1016/j.ijfatigue.2024.108432.
[37] L.C. Andrews, Special Functions of Mathematics for Engineers, SPIE, 1997, https://doi.org/10.1117/3.270709, 1000 20th Street, Bellingham, WA 98227–0010 USA.
[38] Smoothdata Matlab Function, (n.d.). https://es.mathworks.com/help/matlab/ref/smoothdata.html (accessed January 7, 2025).
[39] K. Levenberg, A method for the solution of certain non-linear problems in least squares, Q. Appl. Math. 2 (1944) 164–168. http://www.jstor.org/stable/43633451.
[40] D.W. Marquardt, An algorithm for least-squares estimation of nonlinear parameters, J. Soc. Ind. Appl. Math. 11 (1963) 431–441, https://doi.org/10.1137/0111030.
[41] J.J. Moré, The Levenberg-Marquardt Algorithm: Implementation and Theory, 1978, pp. 105–116, https://doi.org/10.1007/BFB0067700.